Optimization of ICRH for core impurity control in JET-ILW

E. Lerche[1,2], M. Goniche[3], P. Jacquet[2], D. Van Eester[1], V. Bobkov[4], L. Colas[3], C. Giroud[2], I. Monakhov[2], F.J. Casson[2], F. Rimini[2], C. Angioni[4], M. Baruzzo[5], T. Blackman[2], S. Brezinsek[6], M. Brix[2], A. Czarnecka[7], K. Crombé[1], C. Challis[2], R. Dumont[3], J. Eriksson[8], N. Fedorczak[3], M. Graham[2], J. P. Graves[9], G. Gorini[10], J. Hobirk[4], E. Joffrin[3], T. Johnson[11], Y. Kazakov[1], V. Kiptily[2], A. Krivska[1], M. Lennholm[2], P. Lomas[2], C. Maggi[2], P. Mantica[10], G. Mathews[2], M.-L. Mayoral[2], L. Meneses[12], J. Mlynar[13], P. Monier-Garbet[3], M. F. Nave[12], C. Noble[2], M. Nocente[10], I. Nunes[12], J. Ongena[1], G. Petravich[14], V. Petrzilka[13], T. Pütterich[4], M. Reich[4], M. Santala[2], E. R. Solano[15,16], A. Shaw[2], G. Sips[17], M. Stamp[2], M. Tardocchi[10], M. Tsalas[18], M. Valisa[10] and JET Contributors[*]

EUROfusion Consortium, JET, Culham Science Centre, Abingdon, OX14 3DB, UK

[1] *LPP-ERM/KMS, Association EUROFUSION-Belgian State, TEC partner, Brussels, Belgium*
[2] *Euratom/CCFE Fusion Association, Culham Science Centre, Abingdon, United Kingdom*
[3] *IRFM, Association EUROFUSION -CEA, Saint-Paul-Lez-Durance, France*
[4] *Max-Planck-Institut für Plasmaphysik, EUROFUSION -Assoziation, Garching, Germany*
[5] *Consorzio RFX, EUROFUSION -ENEA Association, Padova, Italy*
[6] *Forschungszentrum Juelich, EUROFUSION Assoziation, TEC partner, Juelich, Germany*
[7] *IPPLM, EUROFUSION Association, Warsaw, Poland*
[8] *Association EUROFUSION-VR, Dept. of Physics and Astronomy, Uppsala University, Sweden*
[9] *CRPP-EPFL, Association EUROFUSION - Confédération Suisse, Lausanne, Switzerland*
[10] *Instituto di Fisica del Plasma, EUROFUSION -ENEA-CNR Association, Milan, Italy*
[11] *Association EUROFUSION -VR, Fusion Plasma Physics, EES, KTH, Stockholm, Sweden*
[12] *Instituto de Plasmas e Fusão Nuclear, EUROFUSION -IST Association, Lisbon, Portugal*
[13] *Institute of Plasma Physics, EUROFUSION -IPP.CR Association, Prague, Czech Republic*
[14] *MTA Wigner FK RMI, EUROFUSION Association, Budapest, Hungary*
[15] *LNF-CIEMAT, EUROFUSION Association, Madrid, Spain*
[16] *EUROfusion PMU, Culham Science Centre, Abingdon, OX14 3DB, United Kingdom*
[17] *JET Exploitation Unit, Culham Science Centre, Abingdon, OX14 3DB, United Kingdom*
[18] *FOM Inst. DIFFER, EUROFUSION Association, Nieuwegein, Netherlands*

Abstract. Ion cyclotron resonance frequency (ICRF) heating has been an essential component in the development of high power H-mode scenarios in JET-ILW. The steps that were taken for the successful use of ICRF heating in terms of enhancing the power capabilities and optimizing the heating performance in view of core impurity mitigation in these experiments will be reviewed.

1. Introduction

Since 2011 JET is operating with a full-metal ITER-like wall (ILW), with most of the main chamber plasma facing components made from beryllium (Be) and a tungsten (W) divertor [1]. After an initial period of divertor heat-load investigations and plasma-wall interaction studies [2], JET has entered a phase of high performance scenario development in a full metal environment in view of ITER [3,4]. In H-modes with P_{NBI}>15MW of neutral beam injection (NBI), accumulation of heavy impurities (in particular W) has become a concern, since aside from degrading the plasma performance it can lead to radiative collapse of the discharges, especially when the plasma undergoes a back-transition from H- to L-mode. ASDEX Upgrade (AUG) [5] and more recently JET-ILW [6] experiments have shown that an efficient way of avoiding central impurity accumulation is to provide a localized heat source to the plasma centre, either by electron cyclotron (ECRH) or by ion cyclotron resonance heating (ICRH). The resulting peaked electron temperature profiles, flattened density profiles and enhanced fast ion pressure have a direct impact on the transport of the high-Z impurities in the plasma core, both via neoclassical and via anomalous transport effects [7-11]. Central

[*] See the *Appendix of F. Romanelli et al., Proc. of the 25th IAEA Fusion Energy Conference, 2014, St. Petersburg, Russia*

ICRH as a technique to prevent central impurity accumulation was already applied in JET-C H-mode plasmas with Argon seeding in early 2000 [12].

Currently JET is equipped with four ICRF antennas with a nominal generator power capability of 12MW in ELM tolerant configuration [13]. The actual fraction of the generated RF power effectively delivered to the plasma is lower and depends on the antenna-plasma coupling that, for given RF settings, is dictated by the scrape-off-layer (SOL) density profile in front of the antennas and the pedestal properties, which are usually unfavourable in high power H-mode discharges characterized by low SOL density and steep gradients [14]. The absorption of the waves in the plasma, on the other hand, mainly depends on core parameters such as the bulk plasma kinetic profiles and the minority ion species chosen and its concentration. The typically large temperatures and densities characteristic of high power H-modes are beneficial for efficient RF wave absorption but the actual core electron heating still depends on the slowing-down characteristics of the minority ions and is thus influenced by the minority concentration and the amount of RF power coupled to the plasma [15].

The main results concerning the optimization of ICRH for core impurity control in JET-ILW H-mode plasmas will be summarized. All examples discussed here adopted central H minority ICRH in D plasmas with f=42MHz and B_0=2.7-3.0T. The first step was to increase the power capability of the RF system, by optimizing the RF plant operation and by enhancing the antenna-plasma coupling using localized gas injection (section 2). The second step consisted in optimizing the RF power absorption and core electron heating by fine-tuning the IC resonance position and the minority concentration (section 3). Preliminary work on the minimization of RF-induced impurity sources is described in section 4. Some examples of core impurity mitigation with ICRH in high power baseline H-modes are given in section 5, including a brief discussion about the role of ICRH in assisting a safe H-mode exit and discharge termination. The article ends with a brief summary and perspectives.

2. RF coupling optimization

The first step to improve the application of ICRF heating in high NBI power H-modes was to optimize the RF antenna-plasma coupling to increase the ICRF power capability and reliability in these conditions. This was achieved by tailoring the far-SOL density using dedicated gas injection modules (GIMs) located in the main vacuum chamber as opposed to the default divertor injection usually adopted, as described in [16].

Fig.1 illustrates the impact of divertor (solid) and mid-plane (dashed) deuterium injection in two otherwise similar H-mode discharges: B_0=2.7T, I_P=2.5MA, P_{NBI}=(14±1)MW, P_{ICRF}=3MW, low triangularity. Hydrogen minority ICRF heating with X[H]=n_H/n_e=5% and f=42.5MHz (dipole phasing) was used. The strike point was set on the horizontal divertor target (bulk W) and a 4Hz strike-point sweep was adopted to distribute the heat-load over the divertor stacks. The gas injection rates were similar in the two cases: divertor (1.9×10^{22}e/s), mid-plane (1.7×10^{22}e/s). One sees that switching the gas injection from divertor to mid-plane does not affect the plasma core or the pedestal properties, as seen from the similar line-integrated density and temperature values shown in (a) and (b), respectively. The D_α emission in the outer divertor (c) also indicates similar background neutral pressures (modulated by the strike-point sweeps) and comparable ELM frequencies in the two discharges. The SOL density (d) and the coupling resistances of antennas A and B (e,f), on the other hand, are significantly higher when mid-plane fuelling is used. The effect is stronger for antenna A, which is closer to the gas injection module (~1m), than on antenna B. The SOL density at R=3.88m (~5cm in front of the antenna) is increased by 30-40% when mid-plane injection is used, as measured by a reflectometer located at the same distance from the gas injection point as antenna A (~1m) but in the opposite toroidal direction. Note that the far SOL density and the antenna coupling resistances are quite sensitive to the strike-point position, in particular

with mid-plane fuelling. The maximum in the SOL density / coupling resistance signals occurs when the outer strike point at the horizontal target is positioned furthest away from the vacuum pumping region.

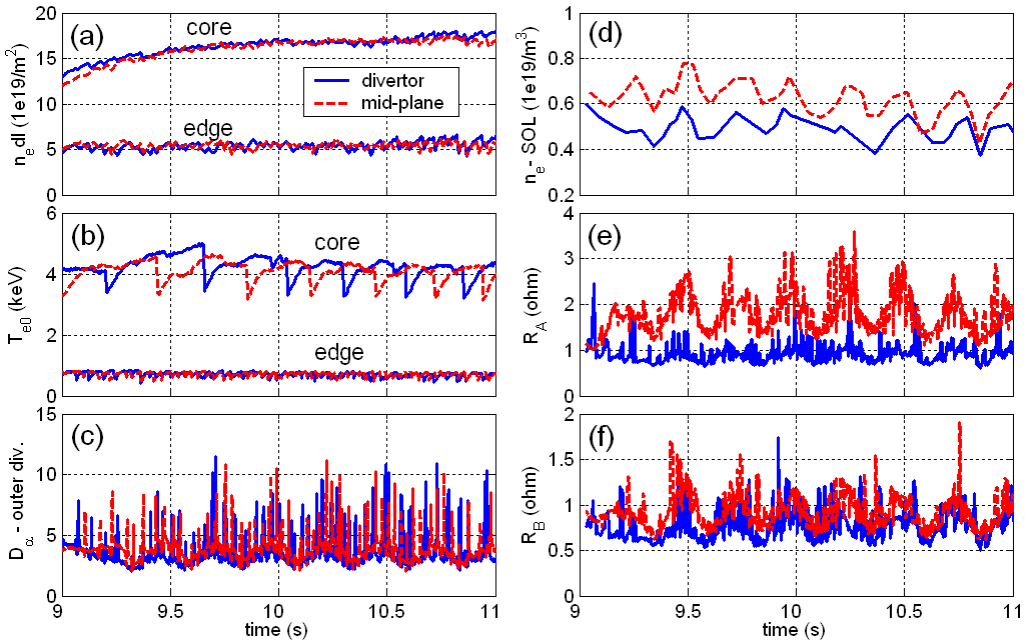

Figure 1: Comparison of two similar H-mode discharges with divertor (solid, JPN84476) and mid-plane (dashed, JPN84478) deuterium injection: (a) Central and edge line integrated electron densities (interferometer); (b) Central and edge electron temperatures (ECE); (c) D_α emission in the outer divertor; (d) SOL density at R=3.88m (reflectometer); (e,f) Coupling resistances for antennas A and B.

A systematic scan of the gas injection options available in JET under similar plasma conditions was performed and the results are summarized in Fig.2, where the mean values of the inter-ELM coupling resistances of the four ICRF antennas (averaged over 1s) are plotted as function of the gas injection rate for different fuelling locations (antennas C and D have the same resistance in ELM-tolerant configuration [17]). All discharges had similar plasma parameters (B_0=2.7T, I_P=2.5MA, P_{NBI}=13-15MW, P_{ICRF}=3-5MW) and f=42.5MHz with dipole phasing was used. Although some changes in the SOL properties were observed, the core and pedestal plasma parameters were not significantly affected by switching the fuelling location in the studied cases: the central electron densities and temperatures were in the range of n_{e0}=(7.0±0.5)x10^{19}/m^3 and T_{e0}=4-5keV, respectively.

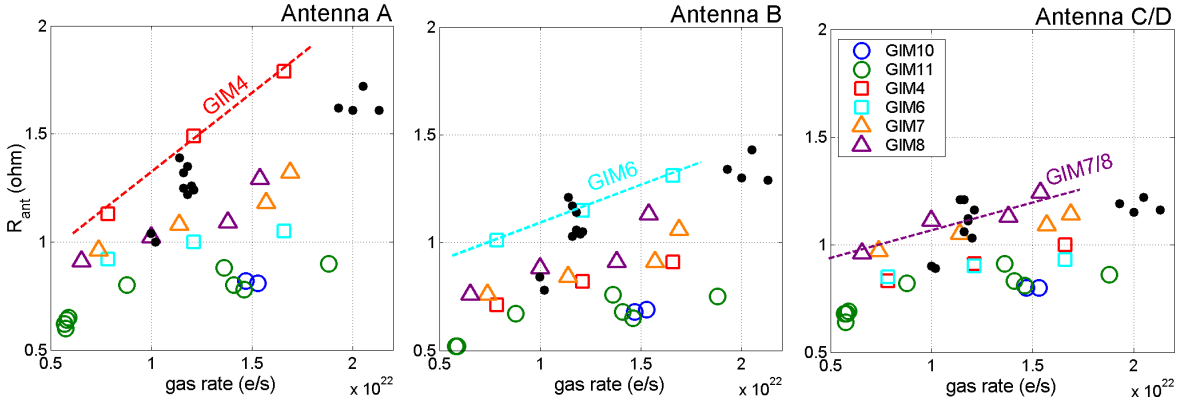

Figure 2: Coupling resistances of the ICRF antennas as function of the gas injection rate for different fuelling locations: Divertor (circles: GIMs 10,11), mid-plane (squares: GIMs 4,6) and top injection (triangles: GIMs 7,8). The data represent 1s averages of the inter-ELM RF signals at constant gas rate. The black dots correspond to the coupling resistances measured when a combination of mid-plane and top fuelling is used (GIMs 4+6+8).

The results show that the strongest coupling enhancement is obtained with mid-plane fuelling close to the antennas (GIM4 is ~1m from antenna A, GIM6 is ~2m from antenna B), suggesting that a local perturbation of the far-SOL density is occurring in these cases. Top injection (GIMs 7,8) has a somewhat weaker impact but it affects all antennas in a similar way, since it leads to a toroidally homogeneous rather than local enhancement of the far-SOL density [16]. Distributed divertor injection (GIMs 10,11) leads to predominantly near-SOL fuelling and thus has the lowest impact on the antenna-plasma coupling and its effect is barely sensitive to the amount of gas injected in the studied discharges. By using a combination of mid-plane and top gas fuelling (black dots in Fig.2), the coupling resistance of all ICRF antennas were simultaneously maximized and ~6MW of ICRF power was reliably coupled to high power H-modes with modest gas injection rates (~$1.2x10^{22}$e/s). Earlier studies performed in AUG have also highlighted the potential of tailoring the SOL density for RF coupling optimization [18]. More recent investigations confirmed the local and global character of the far-SOL density perturbations when respectively mid-plane and top fuelling are used [19].

3. ICRF heating optimization

For given plasma parameters (temperature, density, magnetic field, etc..), the ICRF heating can be optimized by fine-tuning the position of the ion-cyclotron resonance layer and by adjusting the minority (hydrogen) concentration for channelling the absorbed RF wave power to the desired bulk plasma species. The influence of both parameters on the ICRH performance in JET-ILW deuterium H-modes was studied.

3.1 IC resonance position

The ICRF generators in JET only operate at a discrete set of frequencies. Therefore, fine tuning of the ion-cyclotron (IC) resonance position in the plasma has to be done by slightly adjusting the toroidal magnetic field for a given RF frequency. Although it is well known that on-axis ICRF heating has a much stronger impact on the central plasma temperature than off-axis heating, it is not yet clear how central the resonance has to be for impurity control to be achieved. For example, in plasmas with sawtooth activity it is possible that it is sufficient for the RF absorption to be located inside the q=1 surface for efficient central heating to take place due to the fast energy redistribution inside q=1 after a sawteeth crash, as seen in AUG with ECRF heating [20]. From the impurity transport point of view, ICRH should be localized in the region where neoclassical transport dominates over turbulence, in particular if fast ion screening is taken into account. On the other hand, RF-induced turbulent transport in outer regions of the plasma is expected to be less sensitive to the precise location of the RF power absorption and mainly depend on the electron and ion heat fluxes propagating out from the plasma core.

An example of a baseline H-mode discharge (JPN85081) in which the IC resonance was scanned around the magnetic axis (R_0~3m) is given in Fig.3. The RF frequency was f=42.5MHz (dipole phasing) and 3.5MW of ICRF power was applied on top of P_{NBI}=17MW, both applied at t=49s (not shown). Main chamber fuelling with an injection rate of $1.1x10^{22}$ e/s was used and the H concentration was constant around X[H]~5%. One sees that when the ICRF resonance approaches the magnetic axis (t~51.5s), the central electron temperature increases (d) and the inter-sawteeth central SXR emission normalized to the local temperature (e), which indicates core impurity accumulation, is strongly reduced. The bulk plasma radiation (f) is less sensitive to the IC resonance shift and only decreases slightly (~1MW) when ICRH becomes more central. Because the ICRF heating is quite localized in the central region of the plasma (small volume), the total plasma stored energy (c) is not very sensitive to the magnetic field scan. Note that unlike for the SXR signal, the oscillations in P_{rad} are not

related to the ~3Hz sawteeth activity but rather to the 4Hz strike-point sweeps adopted in this pulse for divertor heat-load mitigation.

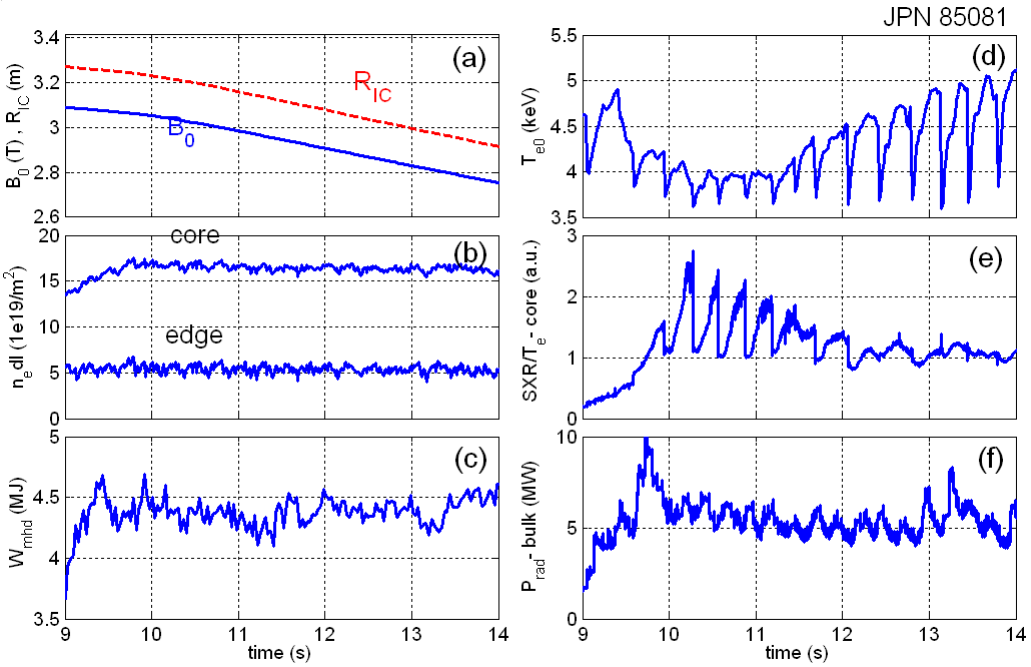

Figure 3: (a) Toroidal magnetic field (solid) and IC resonance position (dashed); (b) Central and edge line integrated electron density (interferometer); (c) Plasma stored energy; (e) Central electron temperature (ECE); (e) Central line integrated soft X-ray emission normalized by the local electron temperature; (f) Bulk radiated power (bolometer). The magnetic axis is at R_0=3m.

The favourable effect of applying ICRH near the magnetic axis becomes more evident when analysing a larger number of discharges as shown in Fig.4, where (a) the central electron temperature, (b) the bulk radiated power and (c) the central soft X-ray (SXR) emission normalized to T_{e0} are plotted as function of the ion-cyclotron resonance position (R_{IC}). The latter was calculated using the total toroidal magnetic field computed by EFIT, which includes paramagnetic corrections (~1-2%). The data represent 0.3s time averaged values in pulses with B_0 scans (2.6T<B_0<3.1T) and otherwise similar conditions: n_{e0}=(7.5±0.5)x10^{19}/m^3, P_{NBI}=15-18MW, P_{ICRF}=4MW, f=42.5MHz (dipole). The magnetic axis is at R_0≈3.0m in all cases and the q=1 flux surface is around 20-25cm off-axis. The normalization of the central SXR radiation with T_{e0} used here as a proxy for the core impurity content is justified at high temperatures (T_e>3-4keV), where high-Z impurity line emission is the dominant contribution to the SXR radiation and the cooling factor is roughly proportional to the local electron temperature [21].

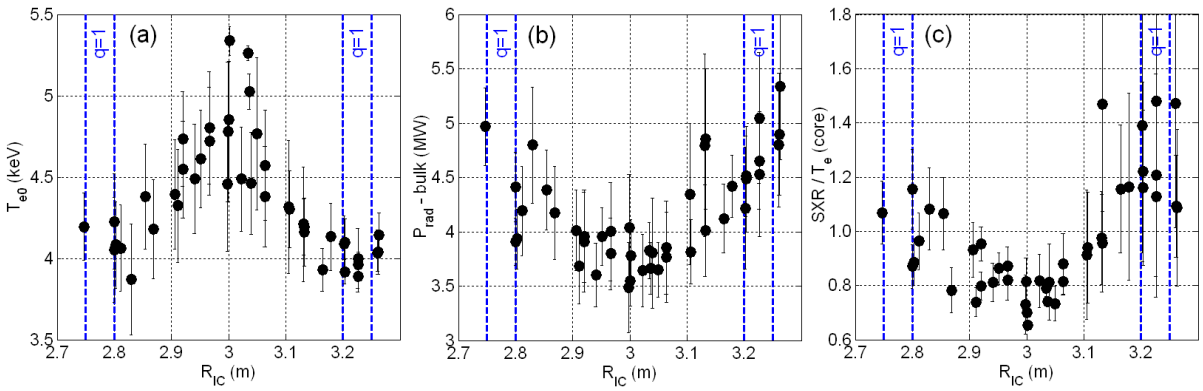

Figure 4: (a) Central electron temperature (ECE), (b) bulk radiated power (bolometer) and (c) central SXR emission (normalized to T_{e0}) as function of the ion-cyclotron resonance position in a series of similar H-mode discharges with 15MW<P_{nbi}<18MW and P_{icrf}=4MW at f=42.5MHz (dipole phasing).

The beneficial effect of applying central ICRH in these discharges is clear: The core electron temperature (a) peaks and both the bulk radiation measured by bolometry (b) and the core SXR impurity emission (c) are minimized when the IC resonance is located within ±10cm from the magnetic axis (2.9m<R_{IC}<3.1m). The bulk radiated power and the normalized SXR radiation in the plasma core are reduced by ~30% when central rather than off-axis ICRH is applied, indicating more efficient impurity screening in these conditions. Although part of this effect is probably related to enhanced neoclassical convection due to larger T_i peaking (not measured), it is believed that fast particle effects, which become more pronounced when the RF power absorption is central (higher RF power densities), are playing a dominant role in the more efficient impurity screening observed when ICRH is central in these conditions.

The strong variation of all quantities with R_{IC} in the region q<1 suggests that it is not sufficient to heat the plasma inside the q=1 surface for impurity mitigation in baseline H-mode plasmas, but rather to apply the ICRF power more centrally. Note that the maximum ICRF power absorption is not necessarily aligned with the cold IC absorption layer: kinetic corrections (Doppler shift) as well as orbit effects can shift the maximum absorption considerably (5-10cm) w.r.t. the cold IC layer in the experimental conditions studied. It has to be mentioned that the averaged values of the central electron temperature and the core impurity content shown in Fig.4 may depend on the sawteeth frequency, which is influenced by the location of the ion-cyclotron resonance w.r.t. the q=1 surface (see the large errorbars when R_{IC} is close to the q=1 surface in Fig.4). Dedicated studies aiming at controlling the sawteeth frequency and simultaneously provide efficient core ICRF heating are ongoing [22].

3.2 Minority concentration

The minority concentration plays different roles in the fundamental ICRF heating scheme: (i) The heating efficiency (related to the single-pass absorption of the waves) is influenced by the minority concentration, since the latter impacts the RF field polarization and consequently the power absorption of the RF waves in the plasma [23]; (ii) The slowing-down of the accelerated H minority ions typically switches from electrons to bulk ions when the minority population is increased, because the fast ion tails created by ICRH are reduced [15]; (iii) The anisotropy of the fast ion distributions is reduced at higher minority concentrations.

The time traces of various quantities in three similar H-mode discharges with different hydrogen concentrations are shown in Fig.5: X[H]=n_H/n_e=6% (solid), X[H]=12% (dashed), X[H]=15% (dash-dotted). The hydrogen concentration was inferred from the ratio between the D_2 and H_2 pressures in the sub-divertor and cross-checked against visible spectroscopy measurements (H_α/D_α), showing an agreement of the order of ΔX[H]=1-2% in the studied range. The main parameters of the discharges were B_0=2.7T, I_P=2.5MA, P_{NBI}=15MW, f=42.5MHz (dipole phasing). Main chamber fuelling with ~1.2×10^{22} e/s was used in the three cases. The step in the ICRF power waveform allows estimating the RF heating efficiency P_{abs}/P_{ICRF}, where P_{abs} represents the 'instantaneous' RF wave power absorption inferred from the response of the plasma energy to the change in input power [24]. One sees that despite the similar core / pedestal electron densities (d), the plasma stored energy is lower for larger H concentrations as a consequence of the poorer RF heating efficiencies observed in these conditions, as discussed later. At high X[H] values, changes in the global plasma confinement can also be contributing to the lower energies reached. The central electron temperatures achieved in steady state (e) are also reduced when X[H] is larger, due to both the lower wave absorptivity and in particular due to the weaker tail formation of the minority H ions, as confirmed by the reduced fast ion flux at E_H=300keV measured by the neutral particle analyzer (f). Note that the sawteeth frequency is not strongly affected by the change in H minority concentration in these examples.

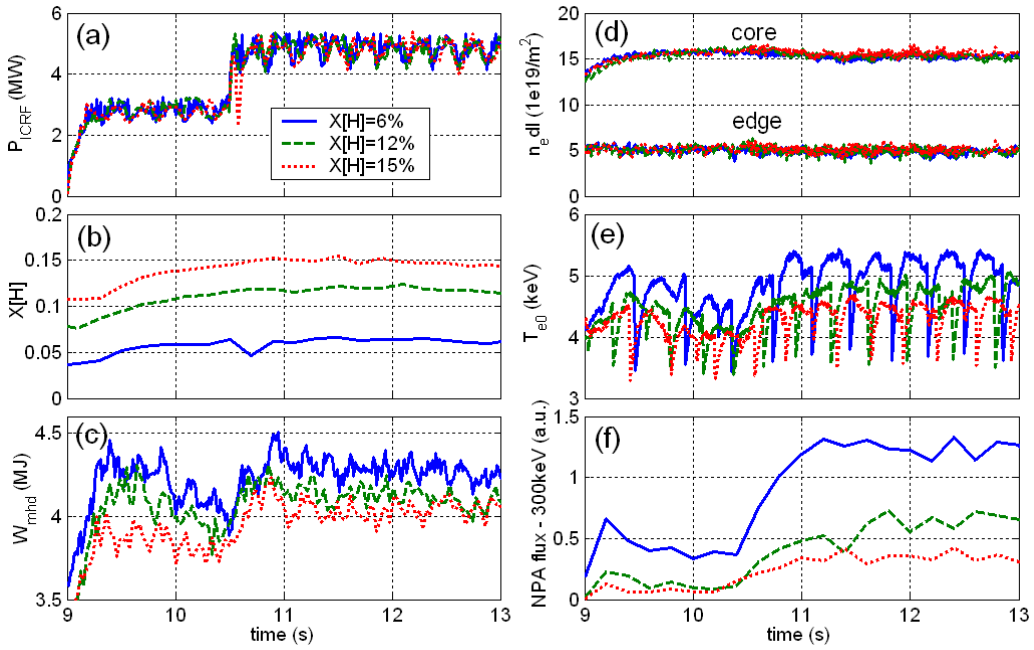

Figure 5: Comparison of three similar H-mode discharges with different H concentrations: X[H]=6% (solid, JPN85379), X[H]=12% (dashed, JPN 85378) and X[H]=15% (dotted, JPN 85373): (a) ICRF power; (b) Hydrogen concentration (pressure in sub-divertor); (c) Plasma stored energy; (d) Central and edge line integrated electron density (interferometer); (e) Central electron temperature (ECE); (f) E_H=300keV hydrogen flux from vertical NPA.

A detailed study of the impact of the H concentration on the ICRF performance in JET-ILW baseline H-modes was reported in [25] and a summary is given in Fig.6, where various quantities are plotted as function of X[H]=n_H/n_e. The RF heating efficiency (a) was estimated from the fast changes of the global plasma stored energy (dW_{MHD}/dt) to RF power steps imposed in the discharges (see Fig.5a). The data on the last two graphs (b,c) correspond to 0.3s time averages of the various signals taken during the flat-top phase of similar discharges with B_0=2.7T, I_P=2.5MA, P_{NBI}=15MW, P_{ICRF}=5MW (f=42.5MHz) and constant plasma density $n_{e0}=(7.0\pm0.5)\times10^{19}/m^3$. The errorbars in the central electron temperature (b) reflect the amplitude of the sawteeth in the various cases.

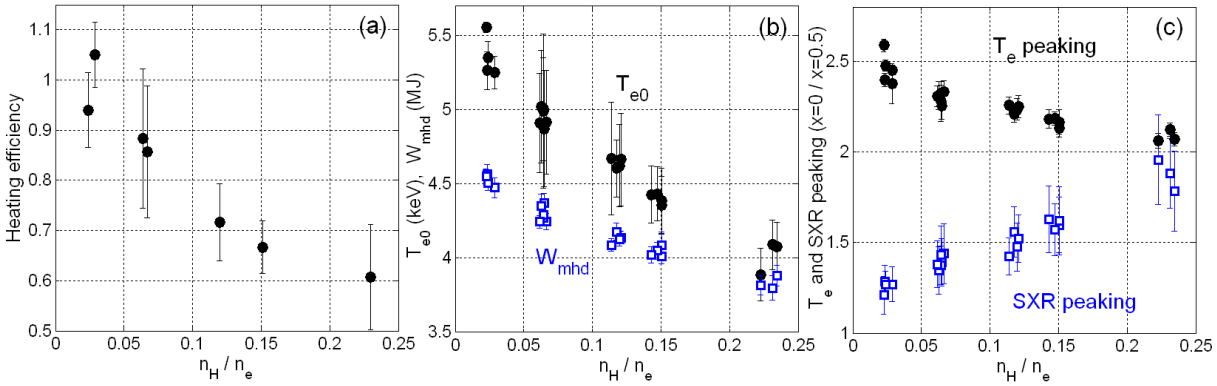

Figure 6: (a) RF heating efficiency estimated from the analysis of the plasma stored energy response to RF power steps as function of the H concentration; (b) Central plasma temperature from ECE (circles) and plasma stored energy (squares) as function of the H concentration; (c) Electron temperature peaking from ECE at r/a=0 and r/a=0.5 (circles) and impurity peaking from SXR measurements (squares) as function of the H concentration. The latter was estimated by the ratio between the line integrated data from vertical SXR channels crossing the mid-plane at r/a=0 and r/a=0.5 normalized by the local temperatures and densities.

The RF heating efficiency (a) decreases from above 0.9 at low H concentrations to approximately 0.6 at X[H]=0.25 and is about 10-20% higher than what was observed in L-mode plasmas in earlier JET-ILW experiments [26]. The main difference is that in H-mode (higher densities) the heating efficiency remains high at low minority concentrations X[H]<0.05, an operational window that is attractive for electron heating from the collisional (slowing-down) point of view and is not available in L-mode. Numerical simulations [27] confirm that the RF wave absorptivity is not degraded at low H concentrations when the plasma density is high and the temperature kept large enough, both due to the reduced wavelength of the fast-wave w.r.t. the ICRF absorption width and the second harmonic parasitic absorption of the NBI D ions, which complements the eventual decrease of the minority H absorption at low X[H]. Both the plasma stored energy and in particular the central electron temperature (b) is reduced at higher X[H] while the impurity peaking inferred from SXR radiation (c) increases. Strong sawtooth stabilization was observed at low H concentrations (X[H]<0.05) but neither deleterious MHD activity nor heavy impurity accumulation were an issue in the studied discharges and the plasma temperature remained sufficiently peaked during the sawtooth-free periods (c).

The fact that the central electron temperature values decay relatively faster than the plasma stored energy when X[H] is increased (Fig.6b) indicates that less RF power is being transferred to the electrons at high X[H] as what would be expected from the decrease in the overall RF heating efficiency only. This is because the slowing-down of the accelerated H ions is gradually shifting from the electrons to the bulk D ions when X[H] is increased due to a reduction of the fast ion tail energies. Oppositely to what was observed in L-mode [25], in H-mode discharges (~2x higher densities) the reduced collisional electron heating at large X[H] is due to a depletion of the number of supra-thermal ions accelerated by ICRH rather than to a decrease of the effective temperature of the fast ion tails.

This is illustrated in Fig.7, where (a) the effective temperature of the fast ion tails $T_{eff}=2/3<E_H>/(k_B n_H)$ and (b) the number of fast H ions with energies between 100keV < E_H < 600keV measured by the vertical neutral particle analyzer (NPA) are shown as function of the hydrogen concentration. In both cases, the NPA measurements were averaged during 1s in the flat-top phase of the discharges with P_{ICRF}=5MW, P_{NBI}=15MW and constant density $n_{e0}=(7.0\pm0.5)x10^{19}/m^3$ (same discharges as in Fig.6). The effective temperatures and number of fast ions were inferred respectively from the logarithmic slope and the flux integral of the NPA energy spectra of hydrogen ions within E_H=100-600keV.

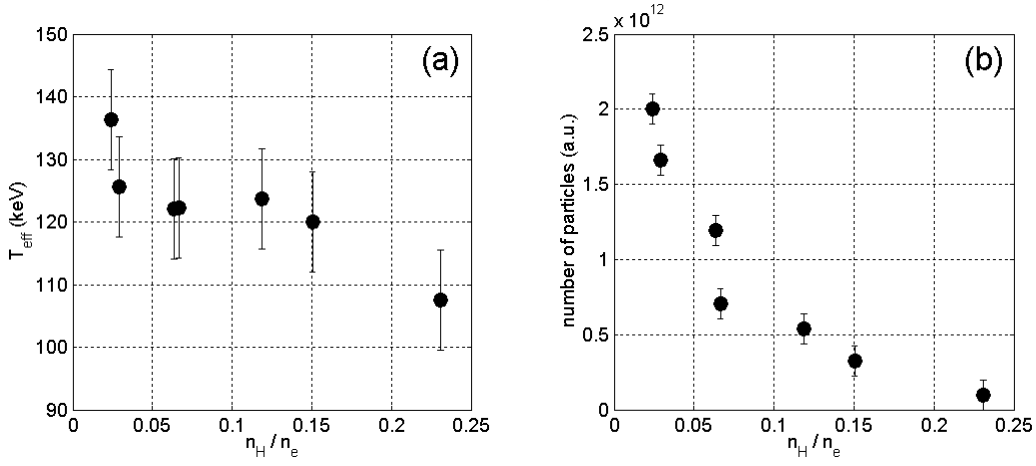

Figure 7: (a) Effective hydrogen tail temperatures and (b) number of fast ions estimated from the fast H ion fluxes measured in the range 100keV < E_H < 600keV by the vertical neutral particle analyzer as function of the H concentration.

One sees that the effective tail temperatures (a) are modest despite the considerable amount of ICRH power applied (as a consequence of the high plasma densities) and that the T_{eff} values do not change much between 2%<X[H]<15%. The number of fast H ions (b), on the other hand, is dramatically reduced when X[H] is increased reaching about 1/4 of its original value at X[H]=2-3% when the hydrogen concentration reaches 12-15%. This behaviour is consistent with 1D Fokker-Planck modelling [28] performed for these plasma conditions.

4. RF impurity source minimization

Although most of the ICRF power absorption does occur in the plasma centre, edge losses associated to RF sheath effects are a major concern when optimizing ICRF heating in tokamaks. Due to the different ion and electron velocities along the magnetic field lines and the low SOL collisionality, the RF electric fields produced by the ICRF antennas induce rectified sheath potentials near the metallic structures [29-33] that can accelerate light ions (such as D, Be, etc.) in the SOL to energies up to a few hundreds of eV, inducing heat loads to plasma-facing components [34-35] and sputtering of plasma-facing material during high power ICRF operation [36-40]. In practice, the additional impurity sources induced by RF sheath effects compete with the beneficial central heating caused by ICRF heating for effective heavy impurity control in full-metal tokamaks. As a consequence, in ICRF assisted JET-ILW H-modes, the total radiation is typically higher than in NBI-only discharges (for same total input power) despite the less peaked radiation and impurity profiles.

The RF sheaths are mainly associated to short wavelength branches parasitically excited by the ICRF antennas and surrounding structures, and thus depend on the antenna geometry, the antenna phasing and the RF frequency. They also depend on the propagating characteristics of the short waves and are therefore also influenced by the far-SOL properties (density, temperature) and by the magnetic field topology of the open field lines. Given the non-linear character of the RF fields in the sheath regions and the entangled magnetic topology connecting the various ICRF antenna arrays with different elements of the first wall, the RF-induced impurity sources are very difficult to localize, characterize and therefore mitigate. The studies performed so far indicate that the main heavy impurities induced by RF sheath rectification effects in JET-ILW are Fe, Ni and W [39], which are sputtered from structures located in the main vacuum chamber (Fe, Ni from Inconel and recessed areas close to the antennas and W from other structures as e.g. the NBI shine-through plates) and from the W-coated upper baffles of the divertor and not from the bulk W divertor itself [38].

The best operational conditions for minimizing the RF-induced plasma-wall interactions in JET-ILW have not yet been systematically identified, but preliminary studies suggest that both the RF antenna settings (phasing, strap voltage balance, etc.) as well as the SOL properties (gas injection, antenna-plasma distance, etc…) can strongly influence the RF-sheath pattern in the SOL.

The effect of RF phasing (dipole=solid, -π/2=dashed) in two similar H-mode discharges with B_0=2.7T, I_P=2.5MA, P_{NBI}=(13±1)MW, X[H]=4-5%, f=42.5MHz is illustrated in Fig. 8. In both cases distributed main chamber fuelling was used with injection rates of $1.2\text{x}10^{22}$e/s (dipole) and $1.45\text{x}10^{22}$e/s (-π/2), respectively. Exciting the RF antennas in dipole phasing ($\Delta\phi=\pi$ between adjacent strap currents) generates a toroidal mode spectrum that peaks at $k_{//,ant}=6.7\text{m}^{-1}$, while current-drive phasing ($\Delta\phi=-\pi/2$) has a maximum around $k_{//,ant}=3.3\text{m}^{-1}$ (longer parallel wavelength). One sees that despite the similar RF power (a) and core plasma properties (b, c), the total bulk radiated power (d) as well as the Ni(e) and W(f) levels near the plasma edge are significantly higher when -π/2 phasing is used once the RF power has stabilized. The fact that the RF-induced plasma-wall interaction is stronger when low $k_{//}$

waves are predominantly excited is consistent with theory [41] and was also documented in detail in JET-C experiments [42-43]. The main difference between the JET-C and the JET-ILW results is the fact that in addition to Ni (and Fe), W sputtering (mainly from main chamber structures and the upper divertor baffles) is also induced by RF-sheath effects. This additional W source - on top of the background W source from the divertor - is significant enough to impact the plasma performance, as seen by the larger mid-radius W concentration measured in the $\pi/2$ phasing case (f). The lower plasma stored energy (c) observed with $-\pi/2$ phasing is also related to the somewhat lower heating efficiency (wave absorptivity) expected for lower $k_{//}$ waves at the given plasma temperature (T_e~5keV), as discussed in [43-44].

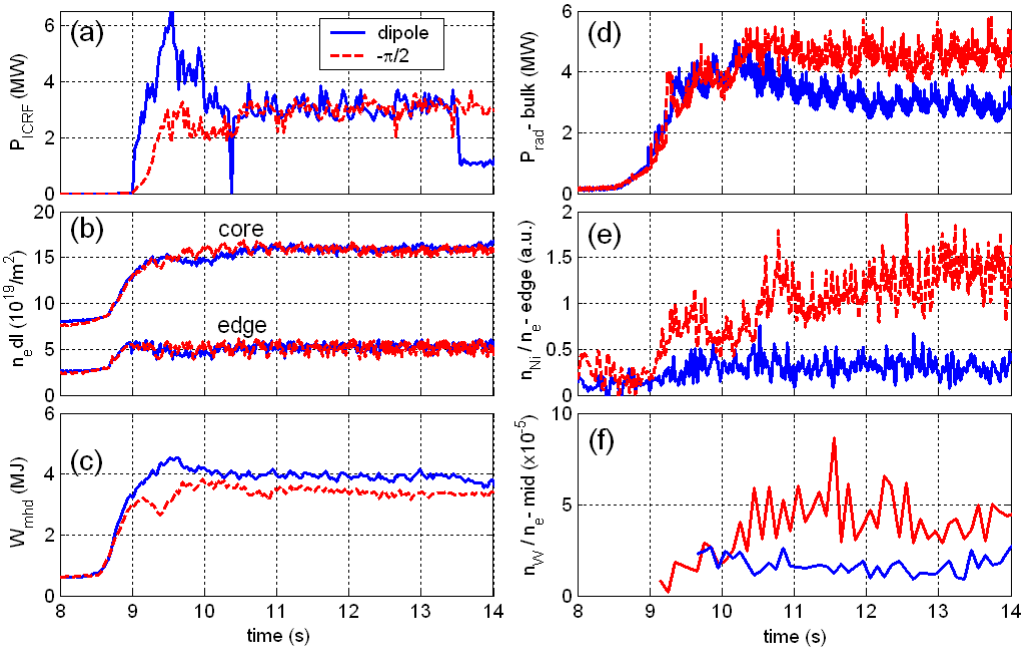

Figure 8: Similar H-mode discharges with dipole (solid, JPN84745) and -π/2 (dashed, JPN84504) RF antenna phasing: (a) ICRF power; (b) (b) Central and edge line integrated electron density (interferometer);; (c) Plasma stored energy; (d) Bulk radiated power (bolometer); (d) Central SXR emission normalized by T_{e0}; (e) edge Ni concentration (a.u.); (f) W concentration at r/a=0.3 (VUV spectroscopy).

An interesting and somewhat non-anticipated result obtained during the coupling optimization experiments was the fact that the RF-impurity sources are reduced when main chamber instead of divertor gas fuelling is used. This is illustrated in Fig.9, where two similar H-mode discharges (the same as shown in Fig.1) with divertor (solid) and mid-plane (dashed) gas injection are compared.

One sees that despite the same ICRF power (a) and similar gas injection rates (b) in the two cases (mid-plane even slightly lower than divertor injection), the edge Ni (e) and W (f) levels are smaller when mid-plane injection is used. As a consequence, the total bulk plasma radiation (c) as well as the central SXR radiation (d) is reduced. Also note that all impurity related signals increase after the gas fuelling is lowered (t=10.5s), as a consequence of the increased sputtering yields commonly observed at lower SOL densities / higher SOL temperatures in JET-ILW and other W-divertor machines [2,38,45].

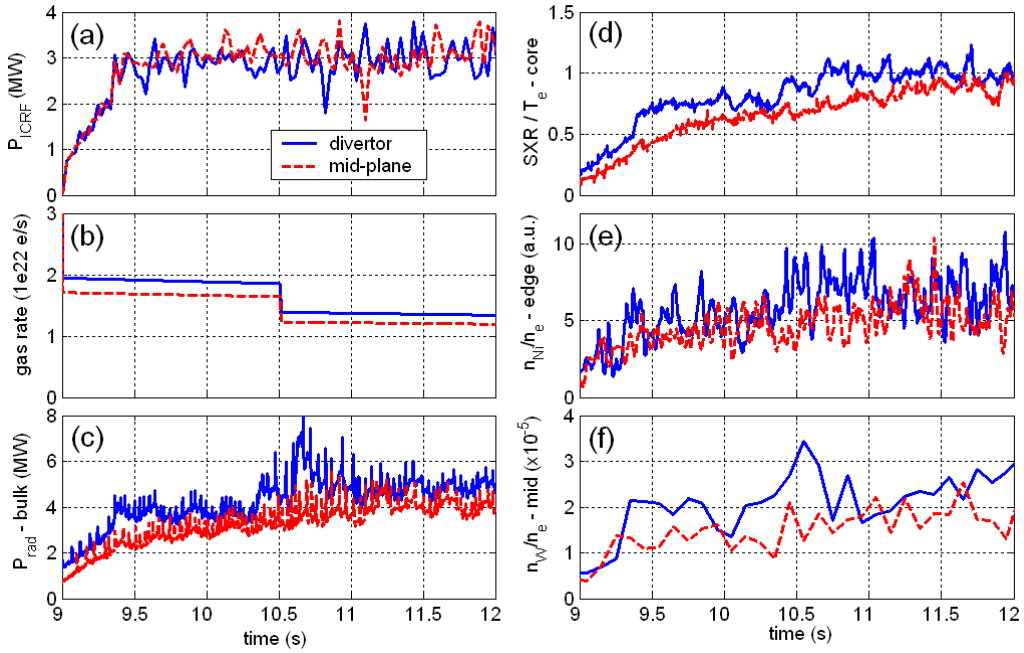

Figure 9: Comparison of two similar H-mode discharges with divertor (solid, JPN84476) and mid-plane (dashed, JPN84478) deuterium injection: (a) ICRF power; (b) Gas injection rate; (c) Bulk radiated power (bolometer); (d) Central SXR emission normalized by T_{e0}; (e) edge Ni concentration (a.u.) and (f) W concentration at r/a=0.3 (VUV spectrometry).

The positive effect of using main chamber instead of divertor fuelling on the RF-induced plasma-wall interaction is summarized in Fig.10, where several impurity related quantities are plotted as function of the gas injection rate for different fuelling cases (same dataset as in Fig.2, B_0=2.7T, I_P=2.5MA, P_{NBI}=13-15MW, P_{ICRF}=3MW, f=42.5MHz). The data represent 1s time averages of the respective ELM-filtered signals taken at constant gas rate.

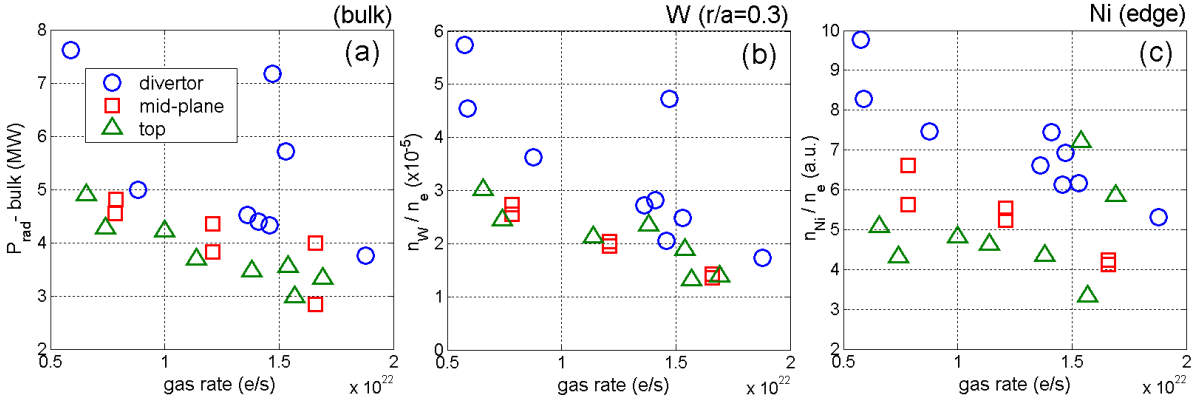

Figure 10: (a) Bulk plasma radiation (bolometer), (b) W concentration at r/a=0.3 (VUV spectroscopy) and (c) edge Ni concentration (VUV) as function of the gas rate for the various fuelling cases studied.

Two features are clearly visible in the results: (i) The bulk plasma radiation (a) as well as the impurity levels (b, c) decrease with larger gas injection in all cases, as the SOL is cooled and the sputtering yield of the ions is reduced. A minimum gas injection level is required to impact on the energy of the impinging ions as seen by the strong increase of all quantities below ~6×10^{21}e/s; (ii) The bulk radiation (a) is lower in the discharges where main chamber gas fuelling is used as opposed to divertor fuelling, in agreement with the lower levels of W (b) and Ni (c) generally observed in these cases. The outstandingly large P_{rad} and X[W] data points in (a,b) correspond to transient W events that occurred in some of the divertor fuelled discharges. These observations suggests that the RF-induced impurity sources are reduced when main chamber fuelling is used w.r.t. divertor fuelling, but changes in the

SOL transport due to the different gas injection location cannot be discarded. A similar effect was observed in AUG when deuterium injection localized close to the RF antennas was used [19,45]. One has to point out that in general, top injection leads to a somewhat higher ELM frequency than mid-plane and divertor fuelling for the same gas injection rate [45,47], which may also contribute to the lower levels of radiation / impurity content observed in the respective data points shown in Fig.10.

The detailed mechanisms that cause the reduction of RF induced plasma-wall interaction when main chamber gas injection is used are still to be identified and require complex modelling of the antenna fields, RF sheath rectification effects and their impact on the SOL particle acceleration and on the wall material sputtering, which is outside the scope of this paper. One effect that most likely plays a role on explaining these observations is that by locally increasing the electron density close to the ICRF antennas, the excited RF fields are reduced leading to lower rectified sheath potentials. Initial simulations performed with a 2D RF wave code that uses a simplified version of the antenna geometry but includes poloidal field effects and adopts a full cold plasma dielectric tensor that describes the excitation of both fast and slow waves [48] confirm a strong reduction of the RF fields when the density in front of the antennas is increased. In these conditions, the parallel component of the RF electric field - believed to be a major player in RF sheath rectification effects – is strongly suppressed, both due to the lower excitation voltages needed per MW of launched power (due to higher antenna-plasma coupling) and in particular due to the increased parallel electron mobility at higher densities. The poloidal component of the RF electric field can also influence the RF sheath rectification in the SOL, either via a direct contribution from its parallel gradients to the process or more indirectly via the induced image currents in the antenna structures and surrounding poloidal limiters, which are both reduced when the antenna-plasma coupling is enhanced due to local gas injection. More detailed modelling including the realistic JET-A2 ICRF antenna geometry as well as experimental SOL density profiles using the TOPICA code [49] are ongoing.

Finally, it has to be mentioned that the mitigation of the RF-induced plasma-wall interaction in high power JET-ILW experiments has only begun and a more systematic study of the influence of the local SOL properties as well as the RF antenna settings (phasing, strap voltage balance, etc.) on the RF sheaths is needed. These studies are planned for the next experimental campaigns in JET-ILW and AUG and will also be pursued on dedicated test-bench experiments specially designed for RF sheath investigations, as described in [50]. Theoretical developments and numerical efforts focusing not only on understanding the underlying RF sheath physics but also on optimizing the antenna design for ICRH systems for future fusion devices are continuing in parallel [51].

5. Examples of ICRH assisted H-modes

ICRH has been an essential tool in the development of H-mode scenarios in JET-ILW due to its potential capability of screening heavy impurities from the plasma core. It is believed that neoclassical effects play the dominant role in the impurity transport near the plasma centre ($r/a<0.3$) whilst turbulent processes become more important for $r/a>0.3$ [9, 10]. ICRH can influence the impurity transport in several ways: (i) Increase the outward neoclassical convection near the plasma centre due to ion temperature peaking and density flattening [52]; (ii) Induce fast particle pressure gradients that cause impurity screening due to collisions between the accelerated minority ions and the heavy impurities [10]; (iii) Generate anisotropic fast ion distributions that can reduce the poloidal asymmetry of the impurities induced by plasma rotation [53-55] and thus reduce the overall neoclassical transport level and enhance the temperature screening factor [56]; (iv) Reduce the toroidal plasma rotation itself due to decreased plasma collisionality [57-59], which again improves the neoclassical

temperature screening and reduces the poloidal asymmetries of the impurity distributions. The relative importance of these processes depends on the plasma equilibrium properties (density, temperature, etc.) and on the characteristics of the RF scheme adopted (minority concentration, location of the IC power absorption, etc.). Furthermore, it is difficult to disentangle the importance of each of the above mentioned mechanisms without detailed measurements of the ion and electron temperatures, the plasma density and the fast particles' characteristics in energy space (tail energies, anisotropy, etc.). Unfortunately, T_i measurements as well as NPA measurements were not readily available in many of the discharges discussed here. Therefore, we will illustrate the effect of ICRH on the impurity transport in terms of a correlation between the SXR impurity peaking and the electron density and temperature peaking. Whilst the former is straightforward (assuming quasi-neutrality), the correlation with T_e peaking has to be interpreted carefully: For high density plasmas (n_e>1e20/m^3), energy equipartion is efficient and the T_e peaking can be more safely used as a proxy for the T_i peaking. For lower densities, the T_e=T_i assumption becomes weaker and the correlation between T_e peaking and impurity screening reflects both T_i peaking and fast ion pressure effects. Again, the actual contribution of T_i and fast particle effects to the T_e and impurity peaking depends on the ICRF absorption characteristics, in particular on the fast ion dynamics and its slowing-down properties.

An example of its influence on a low triangularity H-mode baseline discharge with B_0=2.7T/I_P=2.5MA and similar auxiliary input power (P_{aux}=19MW) is given in Fig.11, where an NBI-only (solid) and an ICRF assisted (dashed) discharge are compared. Both pulses have the strike point located on the bulk W divertor (tile5) with a 4Hz strike-point sweep and identical (main-chamber) gas fuelling with a constant injection rate of 1.2x10^{22}e/s was used. Minority hydrogen ICRH with X[H]=5% and f=42.5MHz (dipole phasing) was adopted and the same amount of hydrogen was injected in the NBI-only pulse for comparison purposes.

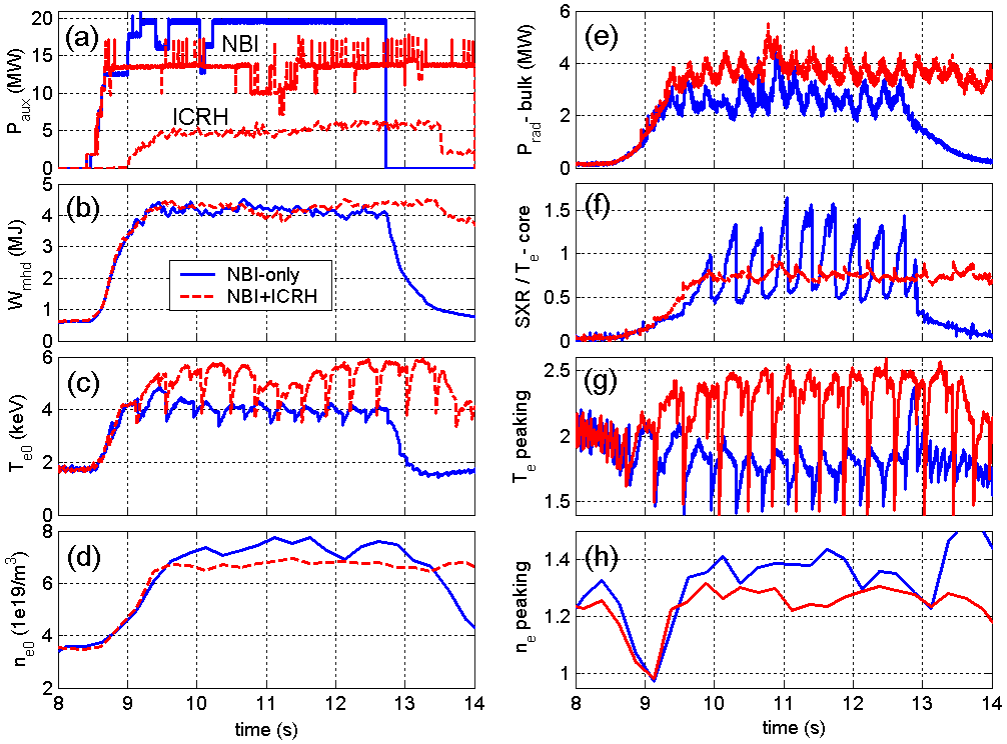

Figure 11: Comparison of two similar discharges with NBI-only (JPN 84746, solid) and NBI+ICRF (JPN 84744, dashed) with the same auxiliary power input: (a) NBI and ICRH power; (b) Stored plasma energy; (c) Central electron temperature (ECE); (d) Central electron density (LIDAR); (e) Bulk radiated power (bolometer); (f) Core SXR emission (normalized to T_e); (g) Electron temperature peaking (ECE); (h) Electron density peaking (LIDAR). The peaking traces represent the ratios of T_e and n_e measured at r/a=0 and r/a=0.5.

In the NBI+ICRH discharge (P_{ICRF}=5-6MW), the central electron temperature (c) is about 1.5-2keV higher than in the NBI-only pulse but the total plasma stored energies (b) are comparable, partly because of the local nature of central ICRF heating (affecting a small volume) and partly because the core plasma density (d) is somewhat reduced when ICRH is applied, as will be discussed later. Although no gradual impurity accumulation is observed in this NBI-only example, the inter-sawteeth impurity peaking is clearly much stronger than in the NBI+ICRH case as seen by the large increase in the core SXR emission (f) and the central temperature saturation during the sawteeth evolution (c). In the NBI+ICRH pulse the normalized central SXR emission is much almost insensitive to the sawteeth oscillations despite their larger amplitude, indicating the absence of heavy impurities in the plasma core. The total bulk plasma radiation (e) is somewhat higher though, reflecting the additional impurity sources induced by sheath effects when ICRH is applied. The less peaked impurity profiles seen in the ICRH assisted discharge are related to the higher T_e peaking (g) and lower n_e peaking (h) observed in this example, which favour the outward neoclassical transport of high-Z impurities near the plasma centre [52]. Dedicated impurity transport studies using W and Mo laser blow-off injection confirm the stronger outward neoclassical pinch in the plasma core when ICRH is applied as compared to NBI-only baseline H-modes [60]. The oscillations seen in the P_{rad} signals (e) are caused by the 4Hz strike point sweeps.

The electron density and temperature profiles achieved in the NBI-only (circles) and in the NBI+ICRH (squares) discharges discussed above are compared in Fig.12 (a) while the impact of ICRF heating on the spatial redistribution of the high-Z impurities in the plasma is illustrated in Fig.12 (b,c), where the 2D tomographic reconstruction of the SXR radiation for the two cases is compared. In both cases most of the impurities are concentrated around mid-radius at the low-field-side of the plasma [61] but in the NBI-only pulse a strong and localized SXR emission is also observed in the very plasma core, confirming that central impurity accumulation is occurring in between sawteeth crashes. In the ICRF assisted discharge, the central emission is largely suppressed but the radiation at mid-radius is enhanced. The fact that the total radiation is higher in the NBI+ICRF case indicates that on top of the high-Z impurity redistribution (from on- to off-axis), additional impurity sources are present when high power ICRH is applied. This highlights once more the importance of mitigating the RF-induced plasma-wall interaction for efficient core impurity control with ICRH in full-metal tokamaks, as discussed in section 4.

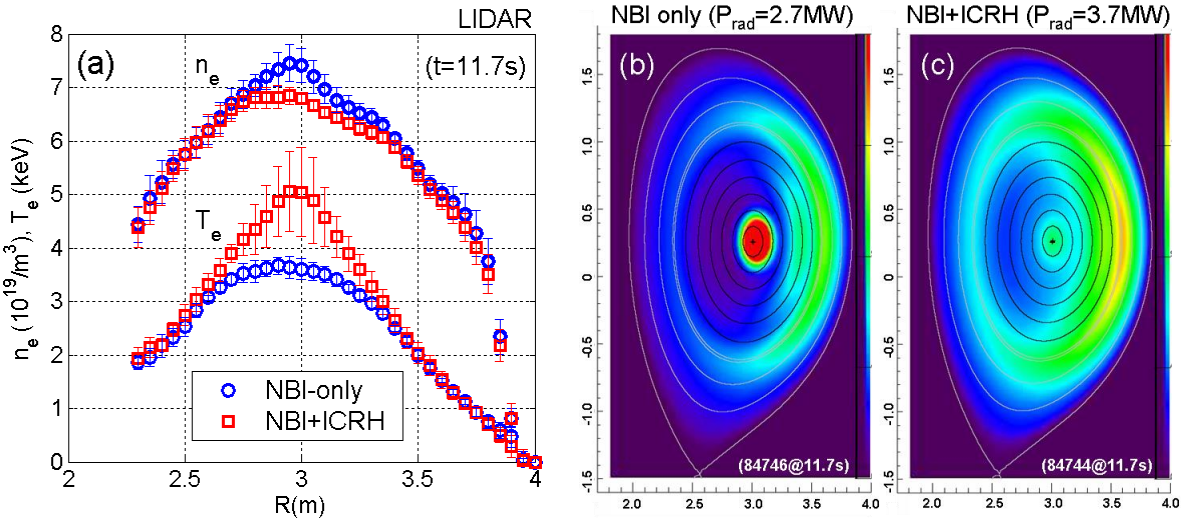

Figure 12: Comparison of two similar discharges with NBI-only (JPN 84746, circles) and NBI+ICRF (JPN 84744, squares) at t=11.7s: (a) Electron density and temperature profiles (LIDAR); (b,c) 2D radiation profiles (SXR tomography). The colorbar is the same for the two radiation graphs.

Dedicated studies of a larger dataset of JET-ILW baseline H-modes reveal that the ability to control impurity accumulation with ICRH is not simply related to the amount of ICRF power coupled to the plasma, but to the impact it has on the core plasma kinetic profiles and on the fast ion dynamics induced by ICRH under different conditions [6, 10]. For example, higher density discharges require more ICRF power to reach similar T_e peaking and fast ion properties (pressure, temperature anisotropy) than low density ones since the fast ion tails and their collisional energy exchange with the electrons is reduced when the background density is higher. On the other hand, collisional bulk ion heating is expected to be more efficient and the T_i profiles could become more peaked and thus directly favour outward impurity convection near the plasma centre.

Fig.13 summarizes the effect of ICRH on the central electron temperature and density values (a), their respective peaking (b) and their impact on core impurity peaking (c,d) in a series of similar high power H-mode discharges with B_0=2.7T, I_P=2.5MA, P_{aux}=15-20MW and n_{e0}=6.5-8x10^{19}/m^3. In all cases central ICRH at f=42.5MHz (dipole) with similar H concentrations (X[H]~5%) was used. All data points correspond to 0.2s time averages of the various signals taken in the different discharges before the sawtooth crashes.

One sees that the central electron temperature (a) increases linearly from around T_{e0}=4keV (NBI-only) to T_{e0}=5.5keV when P_{ICRF}=5MW is applied ($\Delta T/T$~35%) while the central electron density decreases by ~1x10^{19}/m^3 ($\Delta n/n$=12%). The temperature peaking (b), defined here as the ratio between T_e at r/a=0 and at r/a=0.5, increases by ~30% in the same range and mainly reflects the T_{e0} increase with ICRH power. Although the density peaking is ~10% lower in the NBI+ICRH cases than with NBI alone (b), there is only a weak dependence on the ICRH power in the studied cases. The impurity peaking (c) based on (line-averaged) SXR measurements representing r/a=0 and r/a=0.5 is gradually reduced when the ICRH power is increased and for P_{ICRH}>4MW reaching values that are ~2.5 times lower than with NBI alone. Note that in these conditions the impurity peaking is of the same order as the bulk plasma density peaking (~1.25). The large spread in the impurity peaking data for the NBI-only discharges (c) reflects the gradual impurity accumulation observed in some pulses. The correlation between the impurity peaking and the T_e peaking is clear (d) both for the ICRF heated and for the NBI-only discharges: The impurity peaking is reduced by more than a factor of two while the electron temperature peaking increases from about 1.9 to 2.5 with central ICRF heating. Core power balance studies indicate that for most cases the central radiation losses are about one order of magnitude smaller than the external power sources (NBI, ICRH) except for the highest SXR peaking cases with NBI only, where the central radiation losses become non-negligible w.r.t. the heat sources and it is likely that the increased core radiation is contributing to the lower central temperatures (lower T_e peaking) observed, instead of the other way around.

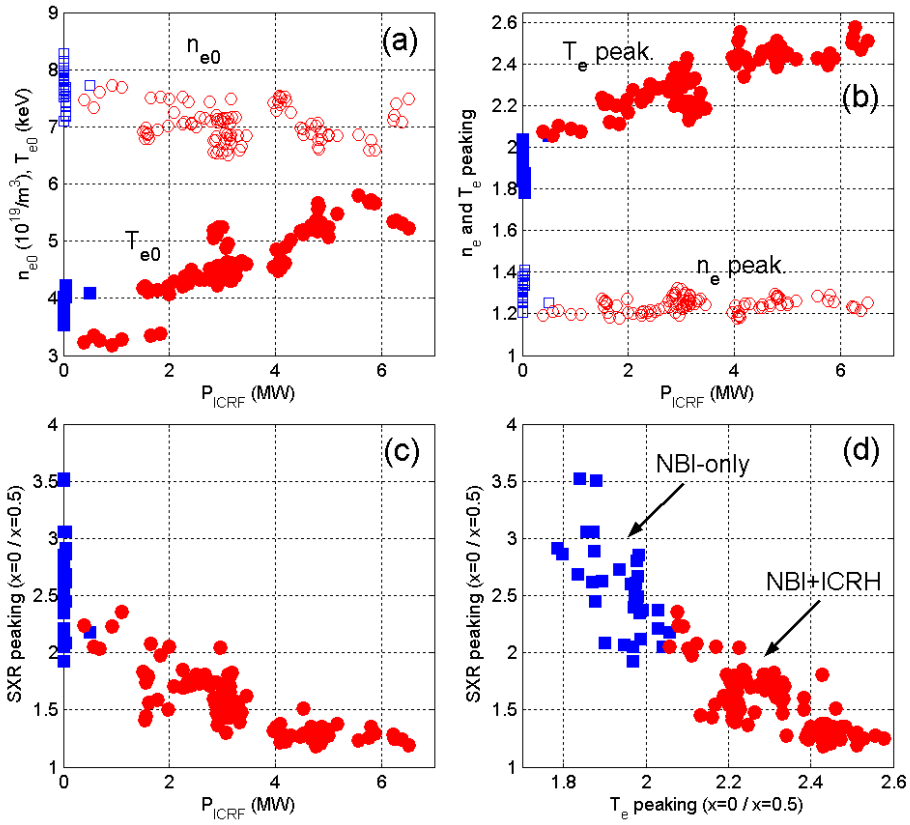

Figure 13: (a) Central electron density (hollow, LIDAR) and temperature (solid, ECE) as function of the coupled ICRH power P_{ICRF}; (b) Electron density (hollow) and temperature (solid) peaking as function of P_{ICRF} (ratios at r/a=0 and r/a=0.5); (c) Impurity peaking (SXR) as function of P_{ICRF}; (d) Impurity peaking (SXR) as function of the T_e peaking shown in (b). The impurity peaking is estimated from vertical line-averaged SXR measurements with line-of-sight crossing the plasma mid-plane at approximately r/a=0 and r/a=0.5, normalized by the local temperatures (ECE) and densities (LIDAR).

The quantity $\nabla n_i/n_i – 1/2 \cdot \nabla T_i/T_i$ is proportional to the ratio between the neoclassical impurity convection and diffusion near the plasma centre in the Pfirsch-Schlüter regime [52], where n_i and T_i are the bulk ion (D) density and temperature values. Here, positive values indicate outward neoclassical convection while negative ones indicate inward convection. If one assumes $n_i=n_e$ and $T_i=T_e$, than the measured electron temperature and density gradients can be directly related to the conditions for core impurity accumulation. As mentioned before, for the ballpark of densities discussed in Fig.13, the $T_i=T_e$ assumption is not necessarily fulfilled and fast ion effects (which are also reflected in the T_e peaking) are probably contributing to the correlation observed between T_e peaking and impurity accumulation. As a crude approximation, one could assume that the kinetic gradients are roughly constant inside r/a=0.5 and use the n_e and T_e peaking values shown in Fig.13(b) to compute the averaged $\nabla n_e/n_e$ and $\nabla T_e/T_e$ terms to compare the differences in the neoclassical transport characteristics when NBI-only and NBI+ICRF are used. For the NBI-only discharges, such estimate gives $R.(\nabla n_e/n_e – 1/2 \cdot \nabla T_e/T_e) \approx 0.3$, which is marginal with respect to neoclassical impurity screening while in the NBI+ICRH pulses, one gets $R.(\nabla n_e/n_e – 1/2 \cdot \nabla T_e/T_e) \approx 1.35$ with $P_{ICRF}>4$MW, which indicates outward impurity convection in these conditions. For these plasmas, the enhanced T_e peaking (and possible T_i peaking) due to ICRH is the dominant effect, contributing to ~70% to the increase in the outward impurity convection when applying ICRH, the other 30% coming from the flattening of the density profile. Fast ion pressure effects are most likely also playing a role in the impurity screening process in these discharges, but low energy NPA measurements were not available in these experiments making it difficult to assess their contribution to the overall impurity transport.

In high confinement discharges such as hybrids [62] and in impurity-seeded H-modes [63, 64], ICRF heating plays an even more important role on the plasma stationarity and on the safe H-L back-transition and subsequent discharge landing. In particular, stationary N_2 seeded H-modes could only be sustained when sufficient amount of ICRH was applied in the discharge. This is illustrated in Fig.14, where an NBI-only (solid) is compared to an NBI+ICRH (dashed) high triangularity N_2-seeded discharge with B_0=2.7T/I_P=2.5MA and similar auxiliary input power (P_{aux}=20MW). The same amount of N_2 ($n_{N2}/n_e \approx 1\%$) was injected in the two cases at t=10s. The strike point is located on the main bulk W divertor (horizontal target) and the usually adopted strike point sweeps were not needed, since the increased radiation caused by the extrinsic impurity injection moderates the divertor heat loads [64]. These discharges are characterized by a higher plasma density than the non-seeded baseline H-modes with similar B_0, I_P and P_{aux} discussed previously.

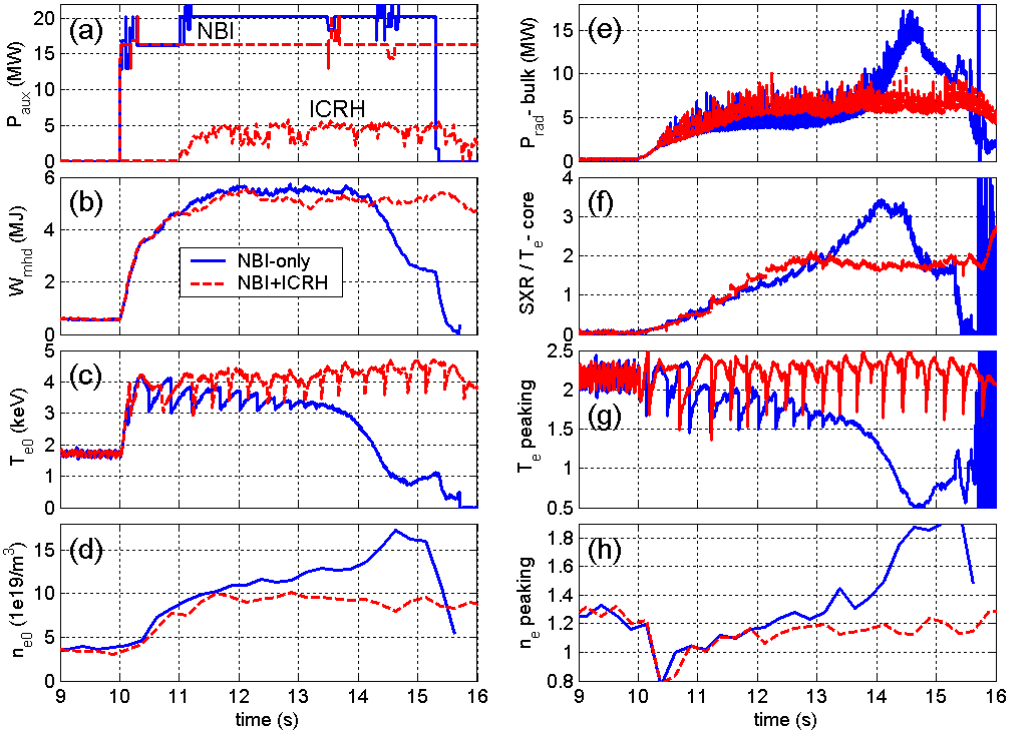

Figure 14: Comparison of two similar N_2-seeded discharges with NBI-only (JPN 85413, solid) and NBI+ICRF (JPN 85412, dashed) with the same auxiliary power input: (a) NBI and ICRH power; (b) Stored plasma energy; (c) Central electron temperature (ECE); (d) Central electron density (LIDAR); (e) Bulk radiated power (bolometer); (f) Core SXR emission (normalized to T_e); (g) Electron temperature peaking (ECE); (h) Electron density peaking (LIDAR). The peaking traces represent the ratios of T_e and n_e at r/a=0 and r/a=0.5.

In this example, the NBI-only discharge does suffer from slow impurity accumulation as seen by the gradual increase of the central SXR emission (f) throughout the pulse and the systematic decay of the central electron temperature (c) and T_e peaking (g), including the eventual suppression of sawteeth at t≈13s. At approximately the same time, the bulk radiation (e) starts to increase and at t≈14s it shoots-up rapidly leading to a radiative collapse of the discharge followed by a disruption. The central plasma density (d) also increases gradually during the pulse from $n_{e0} \approx 1 \times 10^{20}/m^3$ (beginning of the H-mode flat-top) to $n_{e0} \approx 1.2 \times 10^{20}/m^3$ at t=13s and starts to strongly peak afterwards (h). In the ICRH assisted discharge, on the other hand, ~5MW of ICRH power is enough to keep the temperature and density peaking constant during the entire H-mode flat-top at levels that are favourable for neoclassical impurity screening, allowing to reach a high confinement stationary discharge despite of the high levels of central SXR emission and bulk plasma radiation characteristic of seeded plasmas.

Examples of the electron density and temperature profiles for the NBI-only (circles) and the NBI+ICRH (squares) discharges shown in Fig.14 during the healthy plasma phase (t=12.5s) and during the strong impurity accumulation phase (t=14.5s) are given in Fig.15 (a) and (d), respectively. The corresponding 2D radiation profiles of the two discharges inferred from SXR tomography are given in (b,c) and (e,f) for the same time instants.

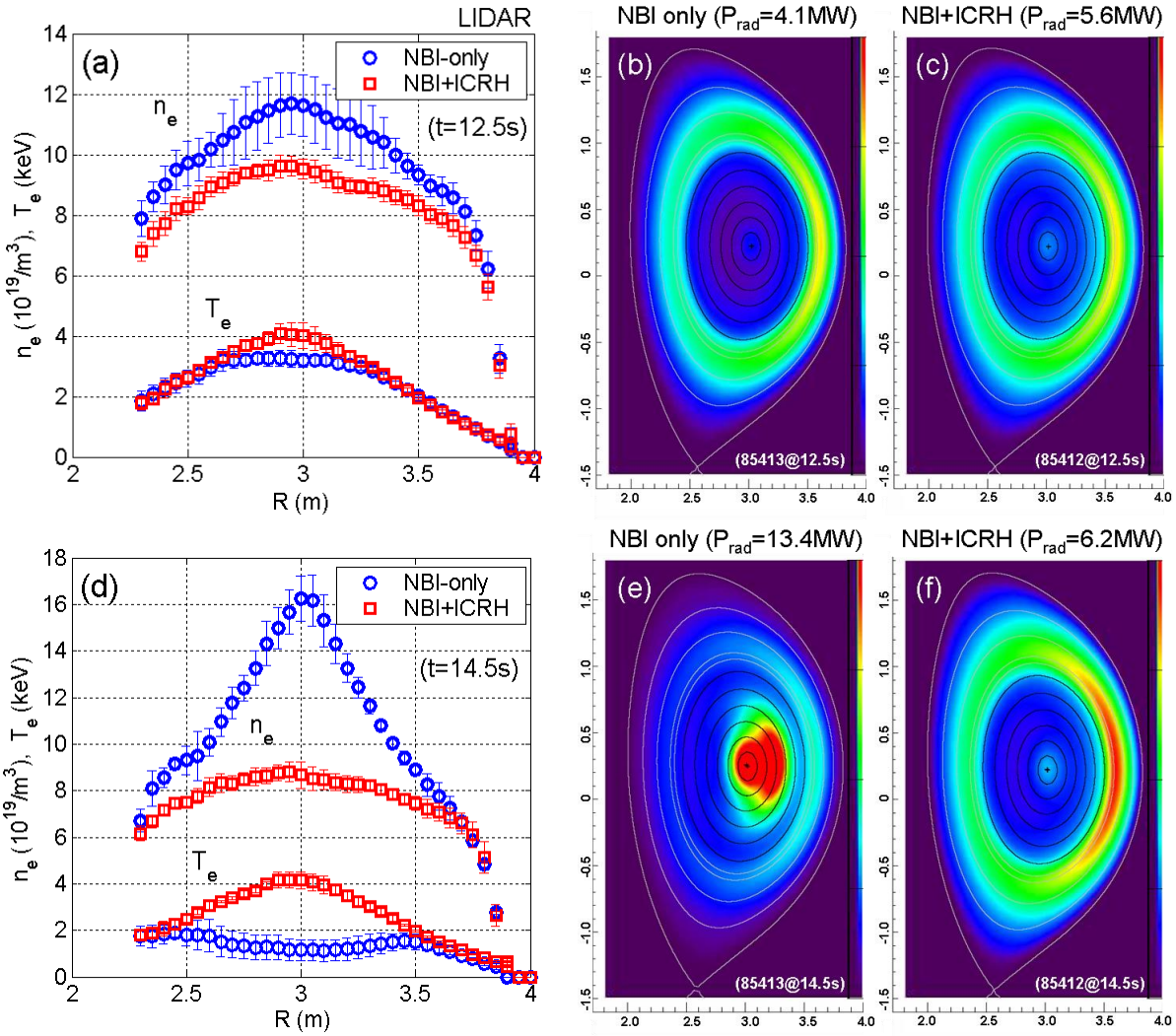

Figure 15: Comparison of two N_2-seeded discharges with NBI-only (JPN 85413, circles) and NBI+ICRF (JPN 85412, squares) at two different time instants: (a) Electron density and temperature profiles at t=12.5s (LIDAR); (b,c) 2D radiation profiles at t=12.5s (SXR tomography); (d,e,f) Same quantities at t=14.5s (during impurity accumulation). The colorbar is the same for all radiation plots.

At the beginning of the H-mode flat-top (t=12.5s), the radiation profiles of the two discharges are similar (b,c) with dominant radiation coming from the low-field-side of the plasma, despite the fact that the electron density is already considerably higher (and somewhat more peaked) in the NBI only case (a). The effect of ICRH on the plasma temperature is modest compared to the non-seeded H-modes discussed before (see Fig.12a) due to the higher plasma densities characteristic of the seeded discharges, and 5MW of ICRH only raises the central temperature by ~1keV. The total radiation is again somewhat higher in the NBI+ICRH case due to RF-induced plasma-wall interaction.

However, the NBI-only discharge is not stationary and at t=14.5s its kinetic profiles are completely different from the NBI+ICRH case (d): The central electron density reaches n_{e0}=1.6x10^{20}/m^3 (~30% higher than at t=12.5s) and the density profile is extremely peaked while the electron temperature has become hollow with central values below T_{e0}<2keV. This

is a consequence of the strong accumulation of heavy impurities in the plasma centre, as seen from the massive core radiation measured in the NBI-only discharge (e). In the NBI+ICRF case, the kinetic profiles remain roughly constant throughout the pulse (the density being even slightly lower at t=14.5s) and the 2D radiation profiles (c,f) are also comparable at the two different instants discussed, indicating that the heavy impurities have been screened from the plasma centre and remain in their original mid-radius position. It has to be noted that the total radiated power is also slightly higher at the later stage of the discharge in the ICRH assisted pulse although there is no indication of slow/systematic increase of the radiated power or the central SXR emission during the discharge (see Fig.14).

A statistical analysis relating the electron kinetic profiles with the applied ICRH power and the SXR impurity peaking was also done for a family of N_2 seeded H-mode discharges. For a better comparison with the non-seeded discharges described earlier (Fig.13), the database only includes pulses with the outer strike point located on the horizontal divertor tiles (high triangularity H3TR configuration) with B_0=2.7T, I_P=2.5MA, P_{aux}=18-22MW, and similar N_2 concentration, X[N_2]=0.8-1.2%. Other seeded H-modes, such as vertical target plasmas, have also been successfully developed with the help of high power ICRH [64] but were not included in the analysis since their plasma properties are quite different from the horizontal target plasma ones described here. The results are summarized in Fig.16, where the central electron temperature and density values (a), their respective peaking (b) and the SXR impurity peaking (c) are plotted as function of the ICRH power applied. In all cases central ICRH at f=42.5MHz (dipole) with similar H concentrations (X[H]=3-5%) was used. The data points represent 0.2s time averages of the various signals taken before the sawtooth crashes.

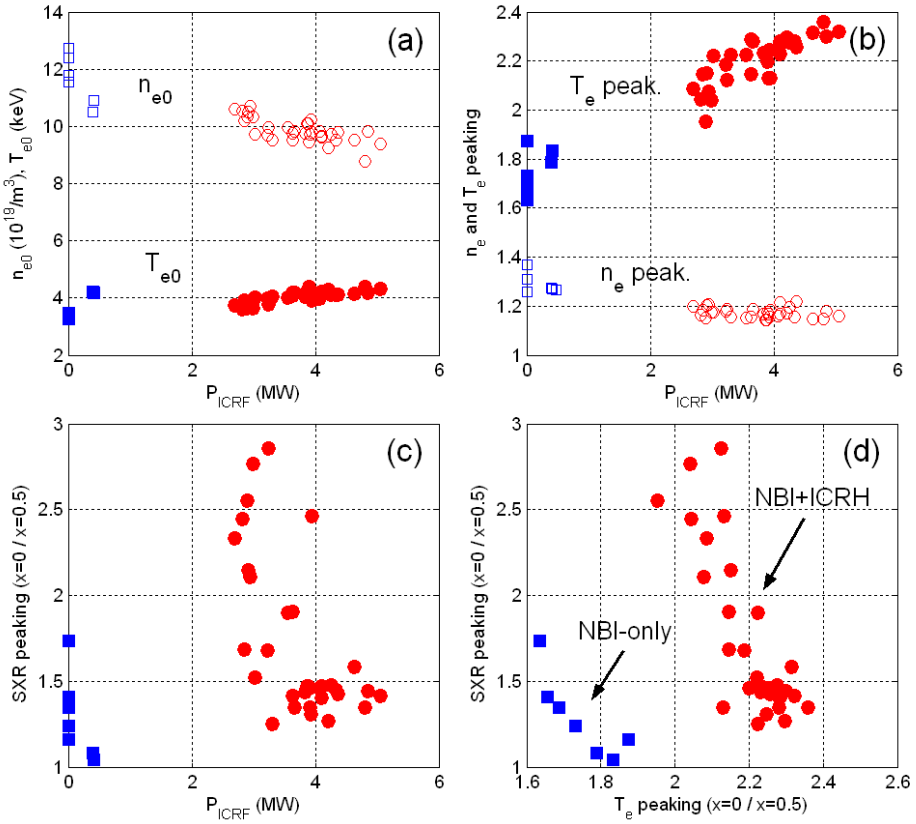

Figure 16: (a) Central electron density (hollow, LIDAR) and temperature (solid, ECE) as function of the coupled ICRH power P_{ICRF}; (b) Electron density (hollow) and temperature (solid) peaking as function of P_{ICRF} (ratios at r/a=0 and r/a=0.5); (c) Impurity peaking (SXR) as function of P_{ICRF}; (d) Impurity peaking (SXR) as function of the T_e peaking shown in (b). The impurity peaking is estimated from vertical line-averaged SXR measurements with line-of-sight crossing the plasma mid-plane at approximately r/a=0 and r/a=0.5, normalized by the local temperatures (ECE) and densities (LIDAR).

In contrast to the results obtained for the non-seeded H-modes (Fig.13), one sees that in these pulses the central density (a) decreases considerably with ICRH power, reaching ~75% of its original value with NBI-only heating ($n_{e0}\approx1.2x10^{20}/m^3$) when P_{ICRF}=5MW is applied. The density peaking (b) is reduced by ~15% (somewhat stronger than in the non-seeded pulses) but is also not very sensitive to the amount of applied RF power. As mentioned before, the central temperature values (a) achieved with 5MW of ICRH power are lower than the ones reached in the non-seeded H-mode discharges (due to the higher plasma densities) but the relative temperature increase is comparable $\Delta T/T\sim30\%$, namely from $T_{e0}\approx3.4$keV with NBI-only to $T_{e0}\approx4.4$keV with P_{ICRH}=5MW. The electron temperature peaking (b) sustained with 5MW of ICRH power (~2.3) is nevertheless slightly lower than the one obtained in the non-seeded discharges with the same power level (~2.5). The impurity peaking dependence on P_{ICRF} (Fig16.c), on the other hand, is very different for the seeded discharges: it does not show a gradual increase when the ICRH power is lower and the T_e peaking is reduced as in the non-seeded examples, but confirms that a minimum power level is needed for avoiding uncontrollable impurity peaking and for sustaining a stationary plasma discharge. The NBI-only examples (squares) can not be compared directly with the ICRF assisted plasma data points (circles), since despite indicating low radiation peaking the overall (on- and off-axis) radiation is much larger than in the NBI+ICRH cases due to strong impurity accumulation. In these cases, core power balance studies suggest that the low central temperatures are a consequence of the core impurity radiation rather than the other way around, as observed in the ICRF heated discharges. Above the RF power threshold, the impurity peaking still seems to correlate with the T_e peaking (d), showing a sharp decrease with ICRH power once the minimum power level has been reached ($P_{ICRF}\sim3$MW). Note that the SXR impurity peaking values obtained in the stationary seeded discharges with $P_{ICRF}>4$MW are about 15-20% larger than the ones achieved at same power level in the non-seeded cases (Fig.13d).

Again, a rough assessment of the electron density and temperature gradients based on the n_e and T_e peaking data (constant gradients inside r/a=0.5 and assuming $n_i=n_e$ and $T_i=T_e$) suggests that the conditions for outward neoclassical convection are not fulfilled in the NBI-only discharges, $R.(\nabla n_e/n_e - 1/2\cdot\nabla T_e/T_e) \approx 0$, but remain quite favourable in the ICRF assisted pulses, $R.(\nabla n_e/n_e - 1/2\cdot\nabla T_e/T_e) \approx 1.5$ for $P_{ICRF}>4$MW. For these discharges (high collisionality) equipartition is strong and the T_e peaking is a good proxy for T_i peaking. In addition, fast particle effects are much weaker in these conditions [10]. Unlike for the non-seeded discharges discussed earlier, for the studied seeded plasmas the contribution of density flattening $\nabla n_e/n_e$ is of the same order as the contribution of the temperature peaking to the increased neoclassical impurity convection obtained with ICRF heating.

The fact that the impurity peaking remains somewhat higher in the stationary seeded H-modes as compared to the non-seeded ones with similar ICRH power despite the comparable kinetic outward neoclassical convection term suggests again that different processes are contributing the to overall impurity transport in the two cases and that a more in-depth analysis is needed to predict the actual W density in the plasma core in a variety of plasma scenarios. For example, the fast ion pressure screening is believed to be lower in the seeded discharges as compared to the non-seeded ones, as a consequence of the reduced H tails at higher densities [10]. For hybrid plasmas, despite of their lower plasma collisionality, the density flattening induced by ICRH is the dominant mechanism affecting the impurity transport [9] and the temperature peaking only plays a minor role. Additionally, recent studies have shown that on top of the local temperature and density profile modification and neoclassical fast ion effects, reduced plasma toroidal rotation and enhanced turbulence induced by ICRH can also contribute to the impurity screening observed with ICRF in JET-ILW H-modes [65, 66].

Parallel investigations have shown that, in general, once the conditions for impurity influx are reached it is difficult to completely reverse the process with the level of ICRF power typically available in high power H-modes (P_{ICRF}≈5MW) and the best results were obtained when ICRH is applied early in the H-mode phase. This is related to the non-linear relation between the density and temperature gradients (which define the neoclassical impurity transport near the plasma centre) and the actual core impurity content, which influences the core kinetic profiles themselves. Therefore, it is important to apply ICRH early enough in an H-mode discharge that is prone to impurity accumulation to allow for the kinetic plasma profiles to reach a favourable equilibrium for impurity screening before the core impurity level is too high. This indicates that the use ICRH in real-time to control impurity peaking requires both early enough detection of the changes in the core impurity distribution as well as enough ICRF power available. Efforts on developing a practical tool for using ICRH in closed-loop to avoid core impurity accumulation are still ongoing [67].

ICRF heating has also shown to play a major role on the H-L back-transition and on a safe termination of the high power H-modes in JET-ILW. Detailed statistical studies indicate that the probability for a disruption to occur during the plasma termination is considerably reduced when even modest amounts of ICRH (2-3MW) are applied during the H-mode exit [68], since the temperature profiles remain peaked during the plasma relaxation after the NBI-switch off avoiding a too strong impurity influx that would otherwise lead to a radiative collapse of the discharge before the plasma current has been sufficiently ramped down.

An example of the positive impact of moderate amounts of ICRH on the H-L transition and the plasma termination is given in Fig.17, where two similar H-mode discharges (B_0=2.65T/I_P=2.5MA) with P_{ICRF}=3MW (dashed) and with shorter P_{ICRF}=1MW (solid) heating are compared. The same amount of gas (~$1x10^{22}$e/s) was injected up to t=20s in the two cases. Note that the plasma current already starts to be ramped-down ~1.5s before the end of the high NBI power phase in these examples.

During the H-mode phase, the two plasmas have similar properties as seen from the comparable central density (d), electron temperature (e) and total bulk plasma radiation (f), although the pulse with 3MW of ICRH shows a somewhat higher radiation near the end of the H-mode flat-top. In the discharge with low (and short) ICRH, the central electron temperature (e) falls very rapidly after the NBI switch-off and leads to a hollow temperature profile after ~0.5s (not shown) while with 3MW of ICRH, the electron temperature is kept in the same ballpark as in the H-mode phase (T_{e0}~4keV) and the T_e profiles are quite peaked. The plasma density, on the other hand, is more peaked in the case with low ICRH, as indicated by the slower density decay after the NBI switch-off (d). As discussed before, these conditions are favourable for inward impurity transport and the bulk plasma radiation (f) is higher in the low ICRH discharge and eventually shoots-up once the ICRF power is completely turned off (t=20s), leading to a disruptive termination of the discharge when the plasma current (c) is only partially ramped down (~2.2MA). In the ICRH assisted case, the electron temperature remains peaked during the transition to L-mode (e) while the density decay is faster (d). In this case, the inward impurity influx is mitigated (f) and a smooth plasma landing is achieved.

The actual amount of power needed for a safe H-L transition depends on the plasma conditions during the H-mode phase (in particular on the plasma profiles and the level of heavy impurities) but in most cases between 2-3MW has been sufficient for a safe plasma termination in most JET-ILW H-modes. Other experiments have shown that, in the case of ICRH unavailability, keeping a few MW of NBI heating during the H-mode exit also helps but because the central electron heating is usually less pronounced, higher amounts of power are likely necessary.

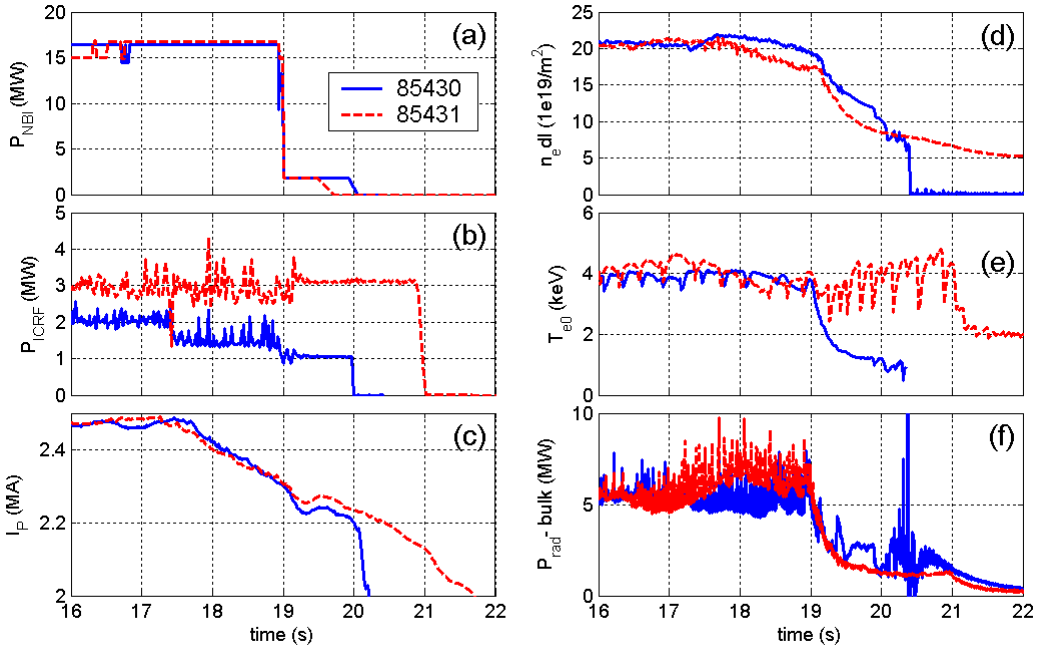

Figure 17: Comparison of the H-L transition and plasma termination of two similar H-mode discharges with P_{ICRF}=3MW (85431, dashed) and with shorter P_{ICRF}=1MW (85430, solid) ICRH: (a) NBI power; (b) ICRH power; (c) Plasma current; (d) Central line integrated electron density (interferometer); (e) Central electron temperature (ECE); (f) Bulk radiated power (bolometer).

6. Summary and Perspectives

ICRF heating is being regularly used in high power JET-ILW H-mode discharges to avoid impurity peaking and to assist on the H-L transition and plasma landing. By using optimized gas injection favourable for RF antenna-plasma coupling based on distributed main chamber fuelling, P_{ICRF}=4-6MW was routinely coupled to high NBI power H-modes, the exact value depending on the plasma configuration and on the gas level used. Preliminary investigations indicate that main chamber fuelling can also potentially help minimizing the RF-induced plasma-wall interaction produced by RF sheath effects, and that dipole antenna phasing performs better than current-drive phasing (lower $k_{//}$). The ICRF heating was optimized in terms of the ion cyclotron resonance position and the minority (hydrogen) concentration. It was seen that central ICRH and low minority concentrations give the best results for core electron heating with absorption efficiencies reaching up to 90%. In these conditions, the peaked temperature profiles (together with relatively flat density profiles) allow efficient high-Z impurity screening to be reached with P_{ICRF}>4MW in most cases.

The study of a large dataset of 2.5MA baseline H-modes with moderate plasma densities (n_{e0}=7-8x10^{19}/m^3) revealed that it is not the amount of ICRF power that actually counts for core impurity control but the ability to sustain sufficiently peaked electron temperatures to favour outward neoclassical impurity convection near the plasma core. For this density range, the increased T_e peaking observed with ICRH and its correlation with the impurity peaking reflects both increased ion temperature gradients (T_e~Ti) and enhanced fast particle effects, which are closely related to T_e peaking via the slowing-down dynamics. In higher confinement regimes such as N_2-seeded H-modes, stationary plasmas could only be achieved when sufficient amount of ICRH was applied early enough in the discharge. In these cases the density flattening induced by ICRH is also plays a significant role in the impurity screening but the impurity peaking still correlates with the T_e peaking above the minimum threshold necessary for plasma stationarity. In these discharges, the plasma collisionality is high (T_i=T_e)

and fast particle screening is strongly reduced so that the correlation between T_e peaking and impurity accumulation mainly represents the effect of the enhanced ion temperature gradients achieved with ICRH. However, it has to be noted that for strong impurity accumulation cases (such as those observed in NBI only seeded discharges), the central impurity radiation losses may become comparable to the central heat sources and in these cases the impurity peaking is the cause for the low central temperatures observed rather than the consequence. Numerical transport modelling suggests that on top of the outward neoclassical convection induced by the favourable density and temperature gradients and the fast particle populations achieved with high ICRH power, other mechanisms such as RF-induced turbulence and reduced plasma rotation with ICRH may also contribute to the impurity screening observed in the ICRF assisted H-modes in general. The relative importance of these processes strongly depends on the specific plasma properties and on the ICRF scheme adopted and detailed studies trying to identify the conditions for which each of these processes is maximized are ongoing.

Preliminary studies of the impact of ICRH on high confinement hybrid discharges and on fully developed (I_P>3MW) baseline H-modes in preparation for DT operation in JET-ILW suggest that 4-5MW of ICRF power is marginal for reliable impurity control but the optimization of the RF heating scenarios in these conditions is still ongoing. In parallel, further optimization of the ICRF system (in particular on the conditioning of the transmission lines and the RF power generators) as well as the reinstallation of the ITER-like antenna [69] are planned for the next experimental campaigns, and are expected to provide the additional amount of ICRH power for a successful exploitation of these scenarios.

The results presented suggest that ICRH can also contribute to high-Z impurity mitigation in ITER, in addition to its traditional role of bulk plasma heating for enhancing the fusion reactions. One important remaining question for JET and ITER DT operations is whether ^{3}He minority ICRH (as opposed to H minority heating described here) also provides efficient impurity screening in high performance H-modes (as expected from theory), a task that will receive strong attention in the next coming JET-ILW experimental program.

Acknowledgements

This work has been carried out within the framework of the EUROfusion Consortium and has received funding from the EURATOM research and training programme 2014-2018 under grant agreement No 633053. The views and opinions expressed herein do not necessarily reflect those of the European Commission.

References

Section 1:
[1] G. Matthews *et al.*, *Phys. Scr.* **2011** (2011) 014001
[2] S. Brezinsek *et al.*, *Journal of Nucl. Materials*, 21st PSI, Kanazawa (2014) (in press)
[3] I. Nunes *et al.*, Proc. of 25th IAEA Fusion Energy Conference, St. Petersburg (2014)
[4] F. Rimini *et al.*, Proc. of 28th SOFT Conference, San Sebastian (2014)
[5] R. Neu *et al.*, *Plasma Phys. Control. Fusion* **49** 12B (2007) B59-B70
[6] M. Goniche *et al.*, Proc. 41st EPS Conference, O4.129, Berlin (2014)
[7] M. Valisa *et al.*, *Nucl. Fusion* **51** (2011) 033002
[8] R. Dux *et al.*, Proc. of 23rd IAEA Fusion Energy Conference, Daejon (2010)
[9] C. Angioni *et al.*, *Nucl. Fusion* **54** (2014) 083028
[10] F. Casson *et al.*, *Plasma Phys. Control. Fusion* **57** (2015) 014031
[11] P. Mantica *et al.*, Proc. 41st EPS Conference, P1.017, Berlin (2014)
[12] M. F. Nave *et al.*, *Nucl. Fusion* **43(10)** (2003) 1204
[13] M. Graham *et al.*, *Plasma Phys. Control. Fusion* **54** (2012) 074011.

[14] E. Lerche *et al., Plasma Phys. Control. Fusion* **53** (2011) 124019
[15] C. Karney, *Comp. Phys. Rep.* **4** (1986) 183

Section 2:
[16] E. Lerche *et al., Journal of Nucl. Materials*, 21st PSI, Kanazawa (2014) (in press)
[17] I. Monakhov *et al., Nucl. Fusion* **53** (2013) 083013
[18] P. Jacquet *et al., Nucl. Fusion* **52** (2012) 042002
[19] P. Jacquet *et al.*, Proc. of 25th IAEA Fusion Energy Conference, St. Petersburg (2014)

Section 3:
[20] J. Stober et al., Proc. of 24th IAEA Fusion Energy Conference, San Diego (2012)
[21] T. Puetterich *et al.*, Proc. of 24th IAEA FEC (2012), San Diego, USA
[221] J. P. Graves *et al., Plasma Phys. Control. Fusion* **57** (2015) 014033
[23] T. Stix, *Nucl. Fusion* **15** (1975) 737
[24] E. Lerche *et al., Plasma Phys. Control. Fusion* **50** (2008) 035003
[25] D. Van Eester *et al.*, in Proc. of 41st EPS Conference, P1.002, Berlin (2014)
[26] E. Lerche *et al., Nucl. Fusion* **54** (2014) 073006
[27] D. Van Eester *et al., Plasma Phys. Control. Fusion* **40** (1998) p.1949
[28] D. Van Eester *et al., Plasma Phys. Control. Fusion* **53** (2011) 092001

Section 4:
[29] D. D'Ippolito *et al., Phys. Plasmas* **13** (2006) 102508
[30] D. D'Ippolito *et al., Phys. Plasmas* **15** (2008) 102501
[31] L. Colas *et al., Phys. Plasmas* **19** (2012) 092505
[32] K. Crombe *et al., Europhysics Conference Abstracts* (2012) series **36F**
[33] D. Van Eester *et al., Plasma Phys. Control. Fusion* **55** (2013) 055001
[34] L. Colas *et al.*, AIP *Conf. Proc.* **1187** (2009) p.133
[35] P. Jacquet *et al., Nucl. Fusion* **51** (2011) 103018
[36] P. Jacquet *et al., Physics of Plasmas* **21** (2014) pp.061510
[37] V. Bobkov *et al, AIP Conf. Proc* **1187** (2009) p.125
[38] V. Bobkov *et al., Journal of Nucl. Materials* **438** (2013) S160–S165
[39] A. Czarnecka *et al., AIP Conf. Proc.* **1580** (2014) p.227
[40] C. Klepper *et al., Journal of Nucl. Materials* **438** (2013) S594–S598
[41] F.W. Perkins, *Nucl. Fusion* **29** (1989) 583
[42] A Czarnecka *et al., Plasma Phys. Control. Fusion* **54** (2012) 074013
[43] R. Weynants *et al., AIP Conf. Proc.* 1187 (2009) p.3
[44] E. Lerche *et al., AIP Conf. Proc.* 1187 (2009) p.93
[45] N. Fedorzak *et al.*, Proc. of 25th IAEA Fusion Energy Conference, St. Petersburg (2014)
[46] V. Bobkov *et al., AIP Conf. Proc.* **1580** (2014) p.271
[47] E. Solano, in Proc. of 41st EPS Conference, P1.006, Berlin (2014)
[48] D. Van Eester *et al., Plasma Phys. Control. Fusion* **55** (2013) 025002
[49] D. Milanesio et al., *Plasma Phys. Control. Fusion* **55** (2013) 045010
[50] K. Crombe et al., Prof of 21st Topical Conf. on RF Power in Plasmas, Lake Arrowhead (2015)
[51] J. Jacquot et *al., Phys. Plasmas* **21** (2014) 061509

Section 5:
[52] S.P. Hirshman and D.J. Sigmar, *Nucl. Fusion* **21** (1981) 1079
[53] M. L. Reinke *et al., Plasma Phys. Control. Fusion* **54** (2012) 045004
[54] C. Angioni *et al., Phys. Plasmas* **22** (2015) 055902
[55] R. Bilato *et al., Nucl. Fusion* **54** (2014) 072003
[56] C. Angioni *et al., Plasma Phys. Control. Fusion* **56** (2014) 124001
[57] L.-G. Eriksson *et al., Plasma Phys. Control. Fusion* **34(5)** (1992) p.863
[58] M.F.F. Nave *et al.*, ECA **31F** (2007) P-4.158

[59] T. Hellsten *et al.*, *Plasma Phys. Control. Fusion* **54** (2012) 074007
[60] M. Valisa *et al.*, Proc. of 25th IAEA Fusion Energy Conference, St. Petersburg (2014)
[61] J. A. Wesson, *Nucl. Fusion* **37** (1997) 577
[62] C. Challis *et al.*, *Nucl. Fusion* **55** (2015) 053031
[63] C. Giroud *et al.*, *Plasma Phys. Control. Fusion* **57** (2015) 035004
[64] C. Giroud *et al.*, *Nucl. Fusion* **53** (2013) 113025
[65] Y. Baranov et al., submitted to *Nucl. Fus.*(?)
[66] J. Citrin et al., *Phys. Rev. Lett.* **111** (2013) 155001
[67] P. Belo et al., Proc. 41st EPS Conference, P1.012, Berlin (2014)
[68] P. de Vries *et al.*, *Phys. Plasmas* **21** (2014) 056101
[69] F. Durodié *et al.*, *Plasma Phys. Control. Fusion* **54** (2012) 074012